Please cite the Published Version

Additional Information: This is an open access article which first appeared in Journal of Magnesium and Alloys
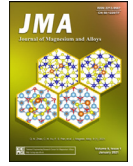
Full Length Article

Tailoring the degradation rate of magnesium through biomedical nano-porous titanate coatings

Matthew D. Wadge [a,*], Jamie McGuire [a], Benjamin V.T. Hanby [a], Reda M. Felfel [a,b], Ifty Ahmed [a], David M. Grant [a,*]

[a] *Advanced Materials Research Group, Faculty of Engineering, University of Nottingham, NG7 2RD United Kingdom*
[b] *Physics Department, Faculty of Science, Mansoura University, Mansoura 35516, Egypt*

Abstract

A novel approach was developed to reduce the corrosion rate of magnesium (Mg) metal, utilising titanate coatings. Magnetron sputtering was used to deposit *ca.* 500 nm titanium (Ti) coatings onto pure Mg discs, followed by hydrothermal conversion and ion exchange reactions to produce sodium and calcium titanate coatings. SEM confirmed the characteristic nanoporous structure of sodium and calcium titanate, with thicknesses ranging from *ca.* 0.8 to 1.4 µm. XPS analysis confirmed the presence of Ti^{4+}—O, Na—O, and Ca—O bonding, whilst Raman spectroscopy demonstrated characteristic vibrational modes (such as TiO_6 octahedral vibrations) of the sodium and calcium titanate perovskite structure. Furthermore, corrosion studies through potentiodynamic polarisation measurements demonstrated the NB/NH CaTC samples to be superior in reducing Mg degradation, compared to other samples tested, through an increase in E_{corr} from −1.49 to −1.33 V, and the reduction in corrosion current density, i_{corr}, from 0.31 to 0.06 mA/cm^2 for Mg and NB/NH CaTC samples, respectively. There was a clear trend noted for the NB/NH samples, which showed an increase in E_{corr} to more positive values in the following order: Mg < Ti coated < NaTC < CaTC. These nanoporous titanate coatings have potential to be applied onto degradable plates for bone fracture fixation, or other orthopaedic applications.

© 2020 Published by Elsevier B.V. on behalf of Chongqing University.
This is an open access article under the CC BY-NC-ND license. (http://creativecommons.org/licenses/by-nc-nd/4.0/)
Peer review under responsibility of Chongqing University

1. Introduction

Magnesium (Mg) has been a material of interest for medical implants due to its low density (1.7–2.0 g/cm^3; cortical bone = 1.8–2 g/cm^3 [1]), and mechanical properties akin to that of cortical bone (Young's Modulus *ca.* 45 *vs.* 5–23 GPa and Ultimate Tensile Strength = *ca.* 160 *vs.* 35–283 MPa, respectively [1]). Its ability to fully degrade in aqueous conditions, and by extension *in vivo*, makes it an ideal biodegradable biomaterial candidate. Furthermore, Mg has found clinical success with MAGNEZIX® MgYREZr; magnesium (Mg), yttrium (Y), Rare Earths (RE), zirconium (Zr), screws as fix-ation orthopaedic devices [2]. However, early investigations of Mg showed that its degradation, while non-toxic, was too rapid for tissue regeneration devices, and the evolution of H_2 gas lead to complications in the healing process of surrounding tissues [3]. To combat these shortfalls, modifications to Mg were investigated within the literature to make it a viable biodegradable implant material. General methods within the literature, to reduce the degradation rate of a biomaterial, have included alloying with other elements, such as zinc (Zn) and calcium (Ca) [4], as well as applying bioactive protective coatings, such as polydopamine [5,6], TiO_2 [5], calcium phosphates/hydroxyapatite (CaP/HA) [7,8], plus others [9].

Of the many different PVD methodologies employed, magnetron sputtering, through the use of permanent and/or electro-magnets to direct secondary electrons produced from

* Corresponding authors.
E-mail addresses: matthew.wadge@nottingham.ac.uk (M.D. Wadge), david.grant@nottingham.ac.uk (D.M. Grant).

plasma-target collisions into a confined area, have demonstrated higher deposition rates [10], as well as decreased operating voltages (typically, -300 to $-500\,V$, compared to -2 to $-3\,kV$) and vacuum pressures (typically, 10^{-3} mbar, compared to 10^{-2} mbar) required for sputtering [11]. Magnetron sputtering also offers coating at low temperatures (< 150 °C), higher coating and plasma densities and the formation of metastable phases [12] further expanding materials available for deposition and substrate selection [13]. These advantages suggest that magnetron sputtering could be an ideal process for production of protective coatings for biomedical materials [14].

A recent study showed that magnetron sputtering allowed deposition of Ti thin films onto alternative material substrates, specifically 316 L stainless steel, and also successfully demonstrated chemical conversion into titanate structures; previously not achieved within the literature [15]. Titanates, initially developed for biomedical applications by Kokubo et al. [16–18], are a class of ceramic materials which enable the production of apatite *in vivo* through the facilitation of several ion-exchange reactions. However, despite extensive research into titanates, both for osteoconductive [19] and antibacterial [20,21] applications, their applicability has been limited to Ti and Ti alloy substrates, due to the chemical conversion route used. Previous work by the authors outlined the potential translation of these surfaces onto alternative substrate materials, for example, onto Mg for corrosion inhibition and improved biocompatibility [15]. This study investigates the production and characterisation of both sodium and calcium titanate surfaces, produced *via* chemical conversion of Ti magnetron sputtered thin films, and their potential application as corrosion inhibitors for biomedical Mg implants. The use of a titanate coating is a novel approach to tailoring the degradation rate of Mg, since the nanoporous titanate structure not only enables enhanced bioactivity of the Mg implant, but will also enable the release of beneficial ions (Na^+ and Ca^{2+}) that can aid in bone growth, and modify the surrounding cellular environment (pH and composition) to prevent Mg degradation; an approach previously not investigated within the literature. Furthermore, the chemical conversion step has also demonstrated the promise for passivation of the underlying Mg, further enhancing corrosion inhibition; suggesting a combinatorial approach.

2. Materials and methodology

2.1. Substrate preparation

2.1.1. Mg discs

A fly press was used to punch Mg discs (10 mm diam., 1 mm thickness, purity: 99.9%, tempered as rolled, Advent Metals Ltd., UK) from an Mg sheet. No further processing of the discs was conducted due to the reactivity of the substrate.

2.1.2. DC magnetron sputtering of CP-Ti thin films

A TEER UDP-650 type 2 unbalanced magnetron sputtering rig with a Ti target ($> 99.6\%$ purity; 175×380 mm)

mounted was used to deposit Ti coatings onto the Mg discs. Mg discs were secured using double-sided polyimide Kapton tape to a rotational (5 RPM) sample holder mounted at a substrate to target distance of 55 ± 1 mm. Ar gas (purity 99.999%; Pureshield BOC) was then introduced a rate of 20 sccm to achieve a working pressure of $<1 \times 10^{-3}$ Torr from the pumped base chamber pressure of $< 1 \times 10^{-5}$ Torr.

Initially samples were bias cleaned with a pulsed DC bias (pulse width of 250 kHz, a step time of 500 ns), at a voltage of $-150\,V$ for 60 min. Discs were then separated into two distinct groups, where differing sputtering parameters were used to determine any effects of film density on the degradation rate. These were designated NB/NH (No Bias/No Heating) and B/300 (Bias/300 °C). The parameters to achieve *ca.* 500 nm thick Ti coatings are detailed in Table 1, utilising previously optimised data for the coating procedure [15].

2.1.3. Sodium hydroxide chemical treatment

A 5 M NaOH solution was prepared by dissolving 19.9 g of NaOH pellets (purity: 99.0%, Sigma-Aldrich) into 100 mL of deionised H_2O. 10 mL aliquots were then poured into polypropylene containers for each sample for conversion. A single Ti-coated Mg disc was placed into each container. Containers were kept in an oven at 60 °C for 24 h. Discs were then removed and rinsed briefly (*ca.* 1 min) in deionised H_2O and then dried in a desiccator. The samples treated this way (NB/NH and B/300) were denoted with the suffix NaTC.

2.1.4. Calcium hydroxide ion-exchange chemical treatment

A 10 mM $Ca(OH)_2$ solution was prepared by dissolving 74 mg of $Ca(OH)_2$ into 100 mL of distilled H_2O. Again 10 mL aliquots were used to submerge the now NaOH-treated substrates (half of the produced NB/NH NaTC and B/300 NaTC samples) in polypropylene containers and heated to 60 °C for 24 h. Discs were then removed from the polypropylene containers and rinsed for *ca.* 1 min in deionised H_2O and then dried in a desiccator. These samples (NB/NH and B/300) were denoted with the suffix CaTC.

2.2. Materials characterisation

2.2.1. Scanning electron microscopy (SEM) and energy dispersive X-ray spectroscopy (EDX)

Imaging of both substrate surfaces and cross-sections were performed with a Field-Emission Gun Scanning Electron Microscope (JEOL 7100F FEG-SEM). A 15 kV accelerating voltage and a working distance of 10 mm, was employed. Cross-sectional images were produced using silica glass discs instead of Mg discs (as used previously [15]), due to the ease of generating sharp cross-sectional fractures and the higher resolution cross-sectional images produced compared to cross-sectional polishing; the glass discs were shattered for cross-sectional analysis. EDX mapping was conducted over *ca.* 100 μm^2 (precipitate analysis) and *ca.* 6 mm^2 areas (delamination analysis) for all samples ensuring a minimum of 250,000 counts ($n = 5$). ImageJ analysis was also conducted on SEM micrographs in order to quantify the level of delamination

Table 1

Coating parameters used for DC Ti magnetron sputtering to achieve a target thickness of *ca.* 500 nm, as optimised previously [15]. NB/NH stands for No Substrate Bias/No Substrate Heating, whilst B/300 stands for −100 V Substrate Bias/300 °C Substrate Heating.

Sample Name	Target Current / A	Substrate Bias / V	Substrate Heating / °C	Coating Time / min	Sputtering Rate / nm.min^{-1}
NB/NH	5	0	0	33.8	14.8 ± 0.11
B/300	5	−100	300	37.9	13.2 ± 0.08

through thresholding the samples and analysing spalled regions through an "Analyse Particle" plugin, determining the average delamination area, frequency, and delamination percentage.

2.2.2. X-ray photoelectron spectroscopy (XPS)

A VG ESCALab Mark II X-ray photoelectron spectrometer with a monochromatic Al Kα X-ray source was utilised for the XPS analysis. Measurements were taken *ca.* 30° incident to the substrate surface. Calibration was carried out through charge correction of the C 1 s photoelectron peak to 284.8 eV in each analysis. Survey scans over a binding energy range of 0–1200 eV were conducted, as well as high-resolution scans for O, Ti, Na, C, and Ca elements. Survey scans were set to a step size of 1.0 eV, number of scans at 5 and a dwell time of 0.2 s, while high-resolution scans used a step size of 0.2 eV, number of scans to 5 and a dwell time of 0.4 s. Resulting spectra were analysed in CasaXPS constraining the Full Width at Half Maximum to the same value for all deconvoluted spectral peaks for the same element, where appropriate. In addition, all *j-j* coupling/spin orbit splitting peaks, most notably the Ti 2p peaks, were constrained to an area ratio of 2:1 for 3/2:1/2 peaks, respectively. Appropriate line shapes were also observed for asymetric metallic *vs.* symetric oxide peak deconvolutions.

2.2.3. X-ray diffraction (XRD)

A Bruker D8 advanced XRD spectrometer (Cu Kα source, λ = 1.5406 Å, 40 kV, 35 mA) was used for determination of substrate crystallinity. To limit the depth of X-ray penetration to the first few microns of the surface, a glancing angle of 1.2° was used. Values of 2θ ranged from 5° to 65°, with a 0.015° (2θ) step size and a dwell time of 12 s.

2.2.4. Raman spectroscopy

A HORIBA Jobin Yvon LabRAM HR spectrometer was used for Raman spectroscopy of the substrates. A 532 nm laser (25 mW power), 300 μm confocal pinhole and 100x objective were used for spectra acquisition. A SYNAPSE CCD detector (1024 pixels) was used for spectra detection, which was cooled to 213 K (−60 °C) thermoelectrically. A 600 lines/mm rotatable diffraction grating along the 800 mm path length was used to achieve detection of multiple Raman shifts simultaneously. The instrument was calibrated with the Rayleigh line at 0 cm^{-1} and standard Si(100) reference band at 520.7 cm^{-1}. The final spectrum for each substrate was a composite of 10 spectra using a 10 s time window.

2.2.5. Electrochemical corrosion testing

Potentiodynamic polarisation (PDP) testing was conducted using a Voltalab PGZ 100 (Radiometer analytical, UK) potentiostat and a three electrode electrochemical cell consisting of, one saturated calomel reference electrode (SCE), one 1 cm^2 Pt auxiliary electrode and one working electrode containing the sample being tested. Each test used 1 L of Dulbecco's Modified Eagle Media (DMEM; MERCK, UK) solution balanced to a pH of 7.4 at 37 ± 1 °C. Open circuit potential (OCP) scans were conducted for 30 min, followed by PDP analysis. Anodic and cathodic scans were conducted from a potential of −2 V to 1.5 V, with a scan rate of 1 mV/s. Tafel analysis (through extrapolation of the cathodic region only due to the Negative Difference Effect of the anodic branch [22,23]) using Voltamaster software determined both E$_{corr}$, i$_{corr}$, and R$_p$ values for each sample, with the tafel region only shown in the figure for clarity.

Additional, qualitative analysis on the potential corrosion rate (v_{corr}), in mm.y^{-1}, was calculated using Faraday's rate equation, according to ASTM G102:89(2015)E1:

$$CR \left(\text{mm.y}^{-1}\right) = K_1 \frac{i_{corr}}{\rho} EW$$

Where *CR* is the penetration rate unit (mm.y^{-1}), i$_{corr}$ (μA.cm^{-2}) is the corrosion current density, K_1 is a constant of 3.27×10^{-3} (mm.g.μA^{-1}.cm^{-1}.y^{-1}), ρ is the materials density (Mg = 1.738 g.cm^{-3}), and *EW* is the 'effective weight', defined as the atomic weight divided by the number of electrons required to oxidise an atom during the corrosion process: Mg = 12.15 [24]. SEM micrographs were also produced for all samples post-electrochemical degradation, and utilised the same parameters outlined in *Section 2.2.1*.

3. Results

3.1. Topographical, structural and compositional analysis

3.1.1. SEM and EDX

Changes in morphology were determined through SEM imaging for all samples in the NB/NH and B/300 sample sets (Figs. 1 and 2, respectively) as well as the Mg control (Fig. 1A insert). The Mg control and the NB/NH Ti and B/300 Ti samples (Fig. 1A insert, Figs. 1A, and 2A, respectively) exhibited relatively smooth morphologies with small cavities present; marginal differences were noted between the samples, however, these were not significant and exemplify the step-coverage of magnetron sputtered coatings.
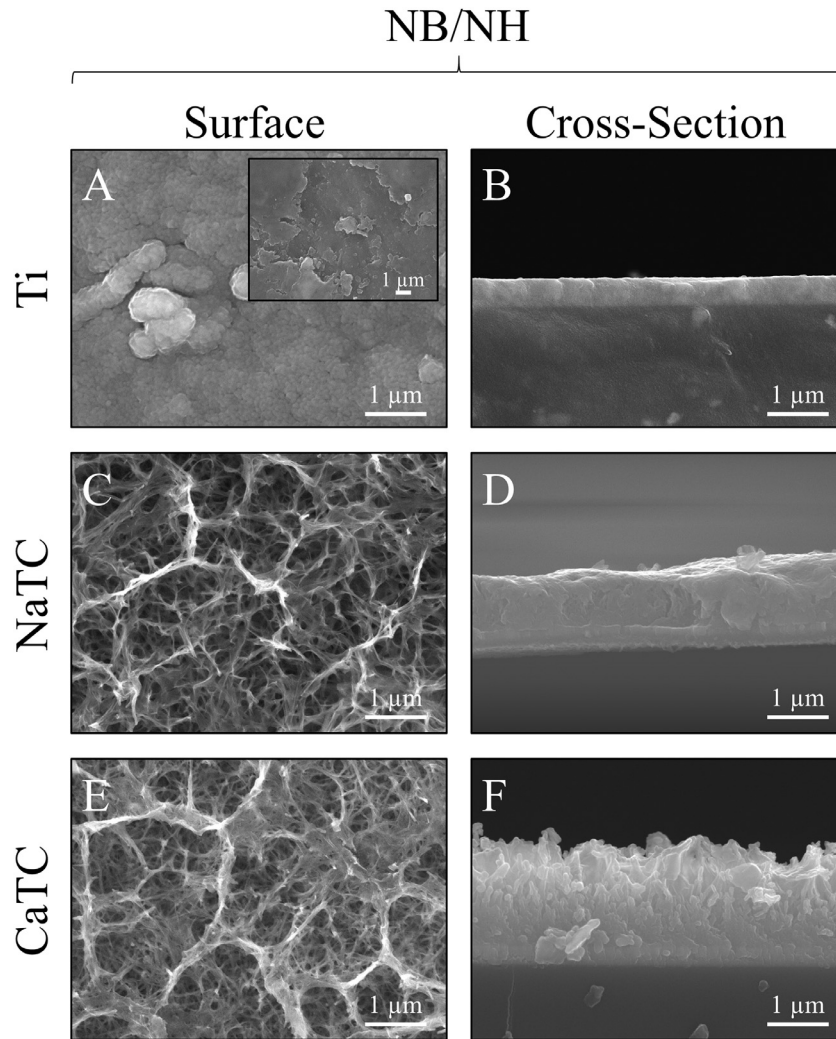
Fig. 1. SEM Surface and cross-section micrographs with A) and B) NB/NH Ti; C) and D) NB/NH NaTC; and E) and F) NB/NH CaTC. Insert micrograph in A) is of the Mg control, for reference.

Table 2

Ti coating and titanate thickness determined via SEM assessment. Error values are standard error; $n = 5$. NB/NH (No Substrate Bias/No Substrate Heating); B/300 (−100 V Bias/300 °C heating); Ti (just Ti coating); NaTC (sodium titanate converted); CaTC (calcium titanate converted).

Sample ID	Total Thickness / μm	Ti Thickness / μm	Titanate Thickness / μm
NB/NH Ti	0.52 ± 0.01	0.52 ± 0.01	N/A
NB/NH NaTC	1.23 ± 0.05	0.29 ± 0.02	0.96 ± 0.05
NB/NH CaTC	1.87 ± 0.12	0.30 ± 0.01	1.42 ± 0.11
B/300 Ti	0.48 ± 0.01	0.48 ± 0.01	N/A
B/300 NaTC	1.57 ± 0.03	0.38 ± 0.03	1.22 ± 0.02
B/300 CaTC	1.11 ± 0.03	0.29 ± 0.01	0.82 ± 0.02

Cross-sectional images show an increase in the overall thickness of the coating when converted from Ti to NaTC, on both the NB/NH (Fig. 1B and D) and B/300 samples (Fig. 2B and D), as well as the appearance of a bilayer in the final coating formed, consisting of Ti (bottom) and titanate (top), distinguished by contrast in intensity and structure; the titanate was nanoporous in morphology compared to the columnar sputter grown Ti coatings. The thickness of both the Ti and titanate portion of the coatings are quantified in Table 2, which showed a decrease in the thickness of the Ti layer in all titanate samples and a significant increase in the total coating thickness due to the titanate growth. Furthermore, the thickness of both NB/NH and B/300 Ti coatings (Table 2) were close to the intended 500 nm coating thickness. The Ti layer revealed a consistent reduction in thickness from *ca.* 500 nm to *ca.* 300 nm for all titanate samples except for B/300 CaTC (Fig. 2F) at *ca.* 380 nm. It was noted that the thickness of the titanate layer showed no pattern between ei-

B/300

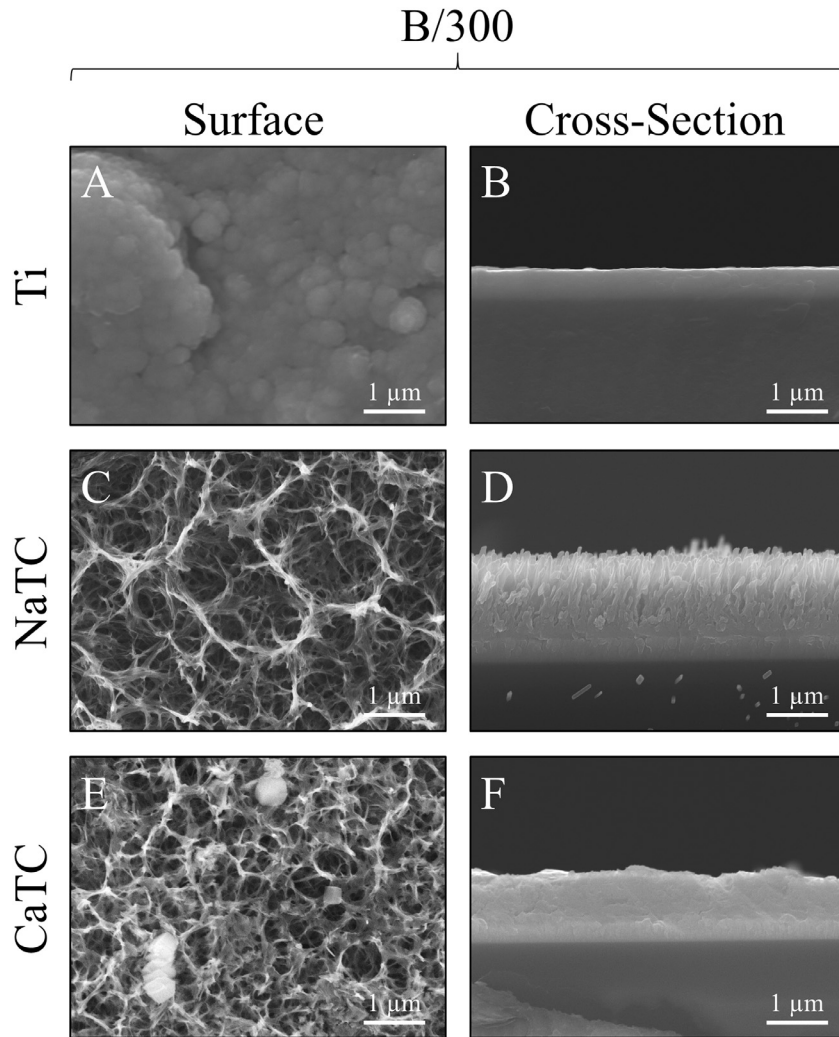|	Surface	Cross-Section

Fig. 2. SEM Surface and cross-section micrographs with A) and B) B/300 Ti; C) and D) B/300 NaTC; and E) and F) B/300 CaTC.

Table 3
EDX elemental data of titanate converted DC magnetron sputtered Ti films. Values given are mean values $\pm$ standard error ($n=5$). All unconverted samples contained 100% Ti via EDX. NB/NH (No Substrate Bias/No Substrate Heating Ti coating); B/300 (-100 V Bias/300 °C heating Ti coating); NaTC (sodium titanate converted); CaTC (calcium titanate converted).

Sample ID	Element quantity / at.%				
	O	Na	Mg	Ca	Ti
NB/NH NaTC	60.2±0.2	8.0±0.2	7.9±0.4	< 0.5	23.4±0.2
NB/NH CaTC	64.2±0.4	< 0.5	6.9±0.2	4.8±0.0	24.0±0.4
B/300 NaTC	59.6±0.6	7.1±0.4	10.4±1.5	< 0.5	22.6±0.7
B/300 CaTC	53.8±2.1	< 0.5	31.5±4.3	3.1±0.6	11.5±1.7

ther sputtering parameters and/or chemical character, with a range of thicknesses from *ca.* 820 nm on B/300 CaTC to *ca.* 1.42 µm on the B/300 NaTC sample.

Analysis of the elemental composition of NB/NH NaTC, NB/NH CaTC, B/300 NaTC and B/300 CaTC samples determined *via* EDX is summarised in Table 3. The O and Ti content were similar for NB/NH NaTC, NB/NH CaTC and B/300 NaTC, while B/300 CaTC showed higher Mg content at 31.5 at.%, correlating with decreased O and Ti content. NB/NH

and B/300 NaTC samples showed an increased Na content (8.0 and 7.1 at.%, respectively) with trace (< 0.5 at.%) Ca content while CaTC samples exhibited the inverse with low Na and higher Ca content (NB/NH $=4.8$ at.%, B/300$=3.1$ at.%). Precipitates on the B/300 CaTC sample were found to be rich in Ca and O, as confirmed *via* EDX (Fig. 3).

EDX mapping (Fig. 4) of the samples suggested partial delamination had occurred in the coatings following wet chemical conversion, particularly for the B/300 NaTC and CaTC
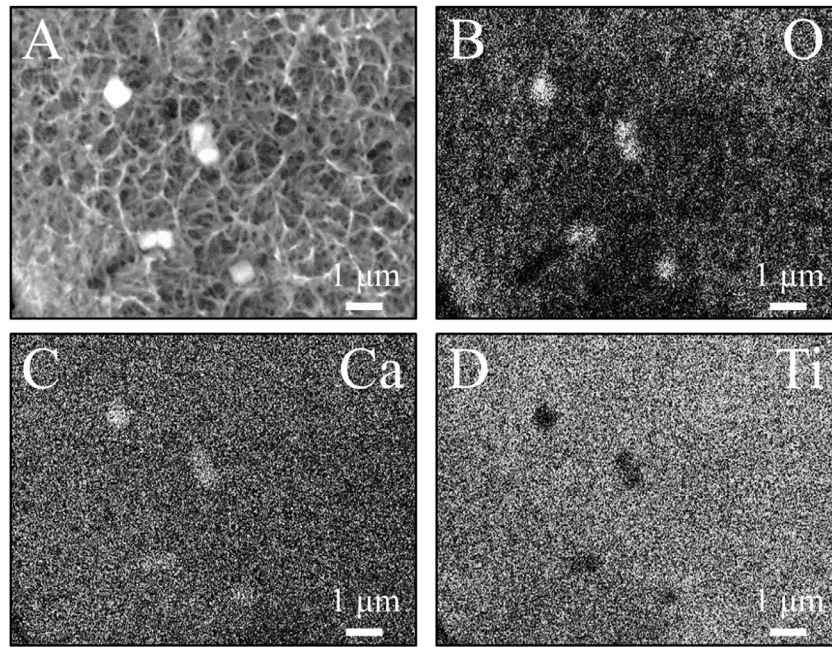
Fig. 3. EDX mapping of precipitates on the B/300 CaTC sample, exhibiting increased intensities of Ca and O, with a reduction in Ti.
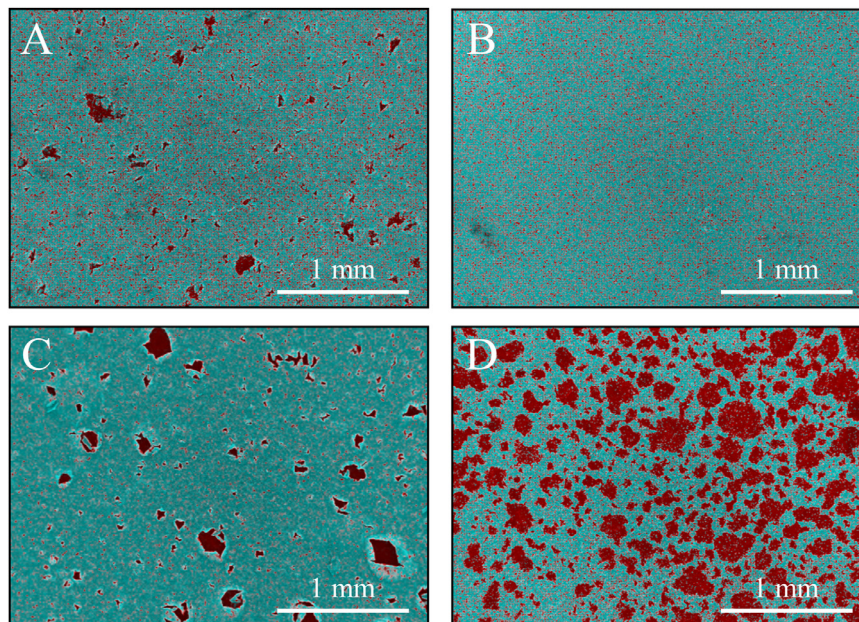

Fig. 4. EDX Mapping of Mg (red) and Ti (blue) overlaying SEM images of delamination (Defined as the clear Mg regions (red) on the EDX micrographs) of A) NB/NH NaTC, B) NB/NH CaTC, C) B/300 NaTC and D) B/300 CaTC. (For interpretation of the references to colour in this figure legend, the reader is referred to the web version of this article.)

samples. Of the coatings produced, the NB/NH samples performed better, with the NB/NH CaTC samples showing minimal delamination ($< 0.1\%$). Delamination data, quantified from ImageJ analysis of the SEM micrographs, which are summarised in Table 4 and indicated the B/300 samples, particularly the CaTC sample, experienced a far higher degree of delamination in total area of delamination (*ca.* 40.3% *vs.* $< 0.1\%$, respectively) and size of delaminated regions (*ca.* 3402.9 μm^2 *vs.* 238.4 μm^2, respectively) than the NB/NH CaTC coatings.

3.1.2. XPS

XPS analysis (Fig. 5) of high-resolution Ti 2p (Fig. 5B), O 1 s (Fig. 5C), Mg 1 s (Fig. 5D), Na 1 s (Fig. 5E), and Ca 2p (Fig. 5F) peaks demonstrated significant differences in peak deconvolutions, spectral shifts, and peak intensities, corresponding to alternative chemical structures produced. All survey spectra (Fig. 5A) detailed noticeable differences between the Ti coated (NB/NH Ti and B/300 Ti), sodium titanate converted (NB/NH NaTC and B/300 NaTC), and calcium ion-exchanged (NB/NH CaTC and B/300 CaTC) samples, however, better comparison can be made in the high-resolution

Table 4

ImageJ quantitative analysis for delamination of titanate coatings on Mg substrates with values given as mean $\pm$ standard error ($n=5$). NB/NH (No Substrate Bias/No Substrate Heating Ti coating); B/300 (-100 V Bias/300 °C heating Ti coating); NaTC (sodium titanate converted); CaTC (calcium titanate converted).

Sample ID	% Delamination (Delamination Area / Total Micrograph Area)	Frequency of Delaminated Regions/mm^{-2}	Average Area of Regions / μm^2
NB/NH NaTC	1.9 $\pm$ 0.7	46.0 $\pm$ 16.8	356.7 $\pm$ 20.1
NB/NH CaTC	< 0.1	0.5 $\pm$ 0.2	238.4 $\pm$ 47.4
B/300 NaTC	6.5 $\pm$ 1.1	40.1 $\pm$ 4.1	1429.1 $\pm$ 126.6
B/300 CaTC	40.3 $\pm$ 6.7	94.5 $\pm$ 5.6	3402.9 $\pm$ 382.3

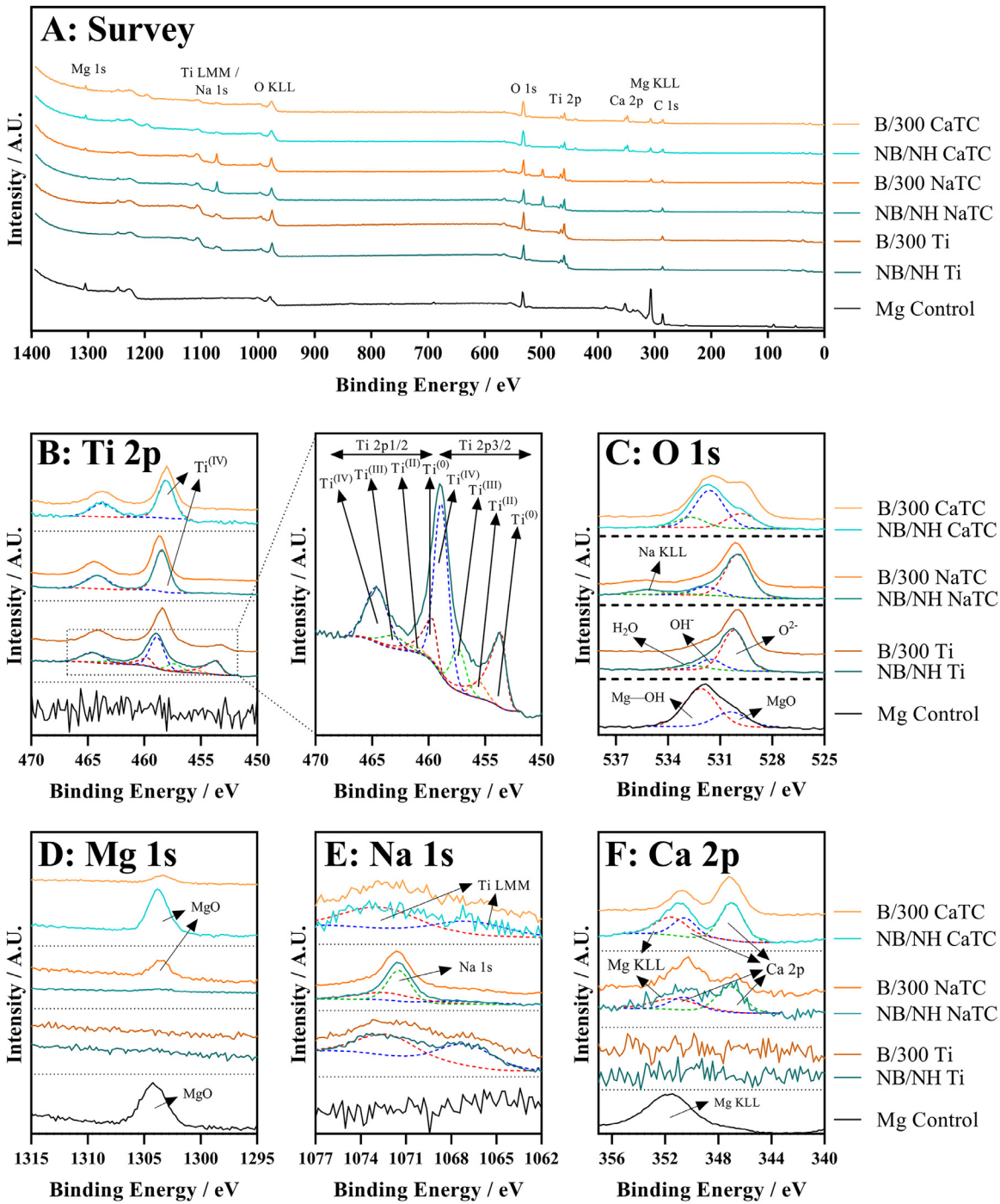

Fig. 5. XPS survey and high-resolution spectra and corresponding peak deconvolutions of Ti coated (NB/NH Ti and B/300 Ti), sodium titanate converted (NB/NH NaTC and B/300 NaTC) and calcium ion-exchanged (NB/NH CaTC and B/300 CaTC) samples. A) Survey, B) Ti 2p with insert spectra showing detailed deconvolutions for the NB/NH Ti sample, C) O 1s, D) Mg 1s, E) Na 1s, and F) Ca 2p elemental peaks.

Table 5

Surface element compositional analysis conducted via XPS survey spectra component fitting. The quoted errors are calculated area standard deviations using CasaXPS. NB/NH (No Substrate Bias/No Substrate Heating); B/300 (−100 V Bias/300 °C heating); Ti (just Ti coating); NaTC (sodium titanate converted); CaTC (calcium titanate converted).

Sample ID	Elemental Composition / at.%				
	Mg	Ti	O	Na	Ca
Mg Control	40.2 ± 0.5	0	59.8 ± 0.5	0	0
NB/NH Ti	0	39.5 ± 0.4	60.5 ± 0.4	0	0
NB/NH NaTC	4.4 ± 0.4	18.0 ± 0.3	59.5 ± 0.6	16.5 ± 0.4	1.7 ± 0.2
NB/NH CaTC	27.0 ± 0.3	4.5 ± 0.2	54.7 ± 0.4	0	13.8 ± 0.4
B/300 Ti	0	31.2 ± 0.5	68.8 ± 0.5	0	0
B/300 NaTC	8.9 ± 0.3	17.5 ± 0.4	51.4 ± 0.9	15.3 ± 0.4	2.0 ± 0.2
B/300 CaTC	11.1 ± 0.3	16.3 ± 0.3	62.6 ± 0.5	0	16.3 ± 0.3

spectra (Fig. 5B-F). The survey spectra was ultimately used to determine the elemental composition of the sample surface's, outlined in Table 5. All samples exhibited some Mg, despite the shallow penetration depth, except for the Ti coated samples. The comparison of NaTC and CaTC samples showed high Na content in NaTC samples becoming zero upon conversion to CaTC, with an associated increase in Ca content. A full account of each deconvoluted peak for each sample is presented in the supplementary information (Tables S1 and S2).

O 1 s high-resolution scans (Fig. 5C) for the Ti coated samples detailed 3 constituent peaks corresponding to O^{2-} (Ti^{4+}—O; *ca.* 71.6%), OH^-/defective oxides (Ti—OH/Ti^{3+}—O/Ti^{2+}—O; *ca.* 18.8%), and H_2O (*ca.* 9.7%). Similar peaks were noted for the NaTC samples with the addition of a peak at 535.2 eV (*ca.* 9%) due to Na KLL Auger electrons. This peak was lost during the conversion to the CaTC samples, with 3 similar deconvoluted peaks to the Ti coated samples corresponding to O^{2-} (Ti^{4+}—O; *ca.* 23–43%), OH^-/defective oxides (Ti—OH/Ti^{3+}—O/Ti^{2+}—O; *ca.* 49–60%), and H_2O (*ca.* 8–16%), although the relative peak intensities/areas were different.

Ti 2p high-resolution analysis (Fig. 5B) corroborated the O 1s findings, with the Ti coated samples (NB/NH Ti and B/300 Ti) exhibiting Ti in all 4 valence states; Ti^{4+} (2p 3/2 *ca.* 458.7 eV; *ca.* 51–64%), Ti^{3+} (2p 3/2 *ca.* 457.2 eV; *ca.* 13%), Ti^{2+} (2p 3/2 *ca.* 455.3 eV; *ca.* 5%), and Ti—Ti (2p 3/2 *ca.* 453.3 eV; *ca.* 17–31%). The number of deconvoluted peaks for Ti 2p doublets decreased to a single doublet for the NaTC (NB/NH NaTC and B/300 NaTC) and CaTC (NB/NH CaTC and B/300 CaTC) samples corresponding to Ti(IV)/TiO_2 (2p 3/2 at *ca.* 458.3 eV); the CaTC samples exhibited a shift (∼ 0.1–0.4 eV) to lower binding energies compared to NaTC samples.

The Na 1s region (Fig. 5E) had an asymmetric peak that resolved into 3 peaks at *ca.* 1071.5 eV (44–53%), *ca.* 1068.2 eV and 1071.5 eV (combined these accounted for the remaining peak area percentage) relating to Na—O and two Ti LMM Auger electron peaks, respectively, for both NaTC samples. For both the Ti coated and CaTC samples, only two constituent peaks were present corresponding to the Ti LMM Auger peaks only. Three peaks were also present in
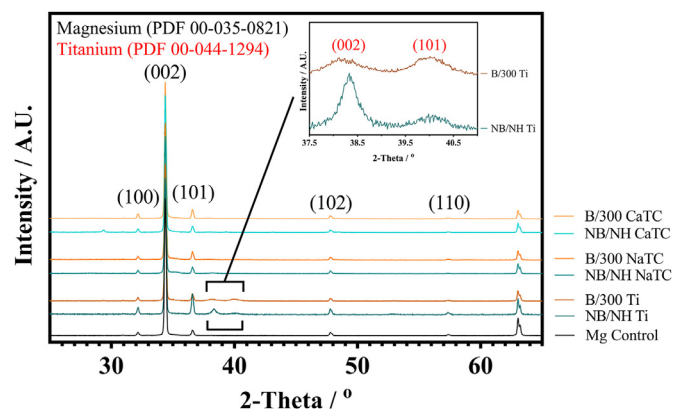

Fig. 6. XRD spectra of all samples types including an insert zoomed in view of two Ti peaks present in both NB/NH Ti and B/300 Ti samples, with annotated crystal planes from Mg (ICDD PDF 00–035–0821; Black) and Ti (ICDD PDF 00–044–1294; Red).

the Ca 2p region (Fig. 5F) for CaTC (NB/NH CaTC and B/300 CaTC) samples attributed to Ca 2p doublets (2p 3/2 *ca.* 347.0 eV; combined *ca.* 67 and 95% for NB/NH CaTC and B/300 CaTC samples, respectively) and Mg KLLb Auger electrons at 351.5 eV (33 and 5% for NB/NH CaTC and B/300 CaTC samples, respectively; a significant increase in the relative quantity of Mg KLL Auger electrons for the B/300 sample is noted).

3.1.3. XRD

XRD analysis (Fig. 6) of the Mg control sample demonstrated peaks at *ca.* 32.2°, 34.4°, 36.6°, 47.8° and 57.4°, which were in good agreement with the ICDD database file for Mg (PDF 00–035–0821) for peak position, however, the peak intensities revealed preferred orientation toward the (002) crystal plane. NB/NH Ti and B/300 Ti coatings exhibited the addition of small, broad peaks at 38.2° and 40.0° corresponding to the ICDD database file for Ti (PDF 00–044–1294) at the (002) and (101) Ti planes, respectively. The NB/NH Ti coating also showed a bias toward the (002) plane, whilst B/300 had an approximately equal split between the two plane orientations. Chemical treatment of both NB/NH and B/300 Ti sputtered coatings resulted in loss of Ti peaks, while Mg
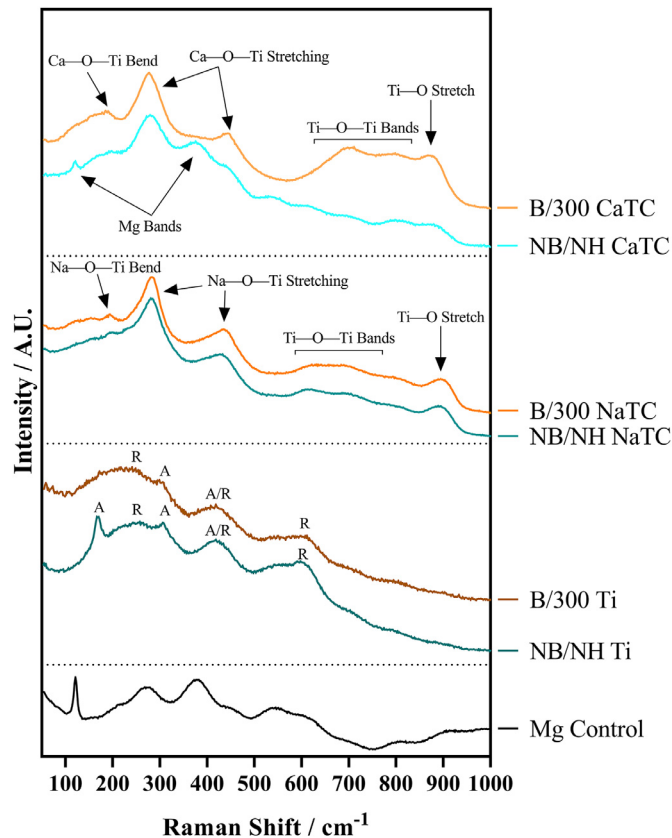
Fig. 7. Raman spectra of all samples with annotated bands. For the NB/NH Ti and B/300 Ti samples, A = anatase and R = rutile.

peaks remained unaltered. No titanate peaks were observed for any of the converted samples.

3.1.4. Raman spectroscopy

Raman spectroscopy (Fig. 7) of the NB/NH Ti samples contained bands corresponding to anatase/rutile mixed phases with bands at *ca.* 169 cm^{-1} distinct to the anatase structure, whilst bands at *ca.* 245, 417 and 600 cm^{-1} are from the overlay of both. NB/NH NaTC and B/300 NaTC samples both demonstrated a band at *ca.* 194 cm^{-1} attributed to the Na—O—Ti bending mode and bands at *ca.* 282 cm^{-1} and 436 cm^{-1} characteristic of Na—O—Ti stretching modes. The band at *ca.* 440 cm^{-1} was characteristic of Ti—O bending, whereby Ti and O atoms were 6- and 3-coordinated, respectively. The band at *ca.* 893 cm^{-1} is due to Ti—O stretching modes, while bands at 625 and 691 cm^{-1} can be assigned to Ti—O—Ti octahedral [TiO$_6$] vibrations.

CaTC Raman spectras differed between NB/NH and B/300 samples, with the NB/NH CaTC sample exhibiting bands associated with the underlying Mg substrate, as described above. However, both samples exhibited the presence of bands at *ca.* 185, 440 and 276 cm^{-1} corresponding to the Ca—O—Ti bending mode and Ca—O—Ti stretching modes, respectively. Additionally bands present at *ca.* 700 and 798 cm^{-1} were suggested to be due to Ti—O—Ti stretching modes, and *ca.* 870 cm^{-1} from the Ti—O stretching mode, emerging within a broad band between 582 and 943 cm^{-1}.

3.2. Combined degradation analysis

3.2.1. Potentiodynamic polarisation analysis

Fig. 8 depicts typical Tafel polarisation curves for the Ti-coated Mg samples (NB/NH Ti and B/300 Ti) and the titanate (NaTC and CaTC suffixes) converted samples. Samples that occupied the lower right quadrant on the graph relative to the Mg control had both lower corrosion current density (i_{corr}) and higher corrosion potential and were thus relatively more stable within the solution with a lower tendency to corrode. It was clear from the data presented that the NB/NH CaTC sample exhibited the lowest i_{corr} and highest E$_{corr}$ values (*ca.* −1.33 V and 0.06 mA/cm^2, respectively. See Table 6) of the samples tested, particularly compared to the Mg control (*ca.* −1.49 V and 0.31 mA/cm^2, respectively) exhibiting the highest i_{corr} and lowest E$_{corr}$ values, respectively. There were clear trends noted for the NB/NH samples, which showed an increase in E$_{corr}$ values in the following order: Mg < Ti coated < NaTC < CaTC. A clear trend due to coating conditions was not observed for the i_{corr} values presented. However, the Ti coated samples, as well as all of the B/300 samples, performed less well compared to the Mg control (*ca.* 0.43 and 0.36 mA/cm^2 for the NB/NH Ti and B/300 Ti samples, respectively, compared to the Mg control at 0.31 mA/cm^2).

3.2.2. SEM of electrochemically degraded samples

Following electrochemical corrosion, the morphological changes occurring on the surface were explored *via* SEM analysis (see Fig. 9). All samples exhibited cracking at the surface, with significant alteration to the surface roughness, anticipated through crevice or pitting corrosion. All titanate converted samples maintained discrete regions characteristic of titanate surfaces, with clear formation of precipitates, in the form of nanoneedles rich in magnesium, chlorine, and oxygen, as detailed from EDX mapping (Fig. S1) exemplified in the B/300 NaTC sample (Fig. 9D), and nano-features rich in calcium, phosphorous, and oxygen on the NB/NH NaTC sample (Fig. 9C).

4. Discussion

4.1. Topographical, structural and compositional analysis

4.1.1. DC magnetron sputtered Ti coatings

Generation of a suitable barrier between Mg and the surrounding extracellular fluid is a complex and demanding challenge in order to mitigate additional necessary surgeries to remove non-degradable fixation devices. This study explored a novel approach for generating bioactive titanate layers onto biodegradable Mg, to facilitate use under *in vivo* corrosion conditions. Recent studies have investigated the potential of titanate layers for increased corrosion protection, such as the study conducted by Arumugam et al., however, the substrate material utilised was a Ti-20Nb-13Zr alloy; a non-biodegradable material [33]. Their study demonstrated improved corrosion resistance of titanate converted surfaces, exemplifying their potential as a corrosion inhibition surface. To
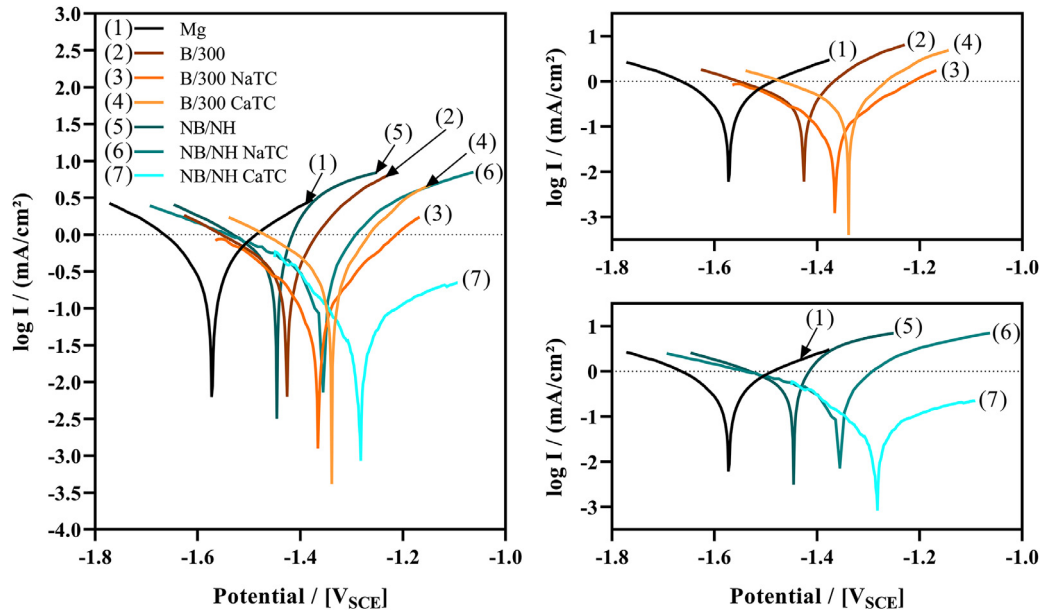
Fig. 8. Representative Tafel plots from potentiodynamic polarisation curves of all coating samples in reference to Mg controls. Left-hand graph combines all samples, whilst the top right and bottom right graphs show localised regions of the B/300 and NB/NH samples, respectively, for better trend observations.

Table 6

E_{corr} and i_{corr} values demonstrating the effect of coating on the degradation rate of Mg. Error values are standard error; $n = 3$. The values for pure Mg have been compared with similar studies within the literature and are within an agreeable tolerance despite the variance in testing methodologies [25–32].

Sample ID	Corrosion Potential, E_{corr} / V	Corrosion Current Density, i_{corr} / (mA.cm^{-2})	Polarisation Resistance, R_p / $\Omega.cm^2$	Corrosion Rate, v_{corr} / mm.y^{-1}
Mg	-1.49 ± 0.07	0.31 ± 0.09	155.8 ± 48.7	6.96 ± 0.01
NB/NH Ti	-1.48 ± 0.01	0.43 ± 0.14	128.8 ± 66.3	9.88 ± 0.01
NB/NH NaTC	-1.34 ± 0.07	0.22 ± 0.08	204.2 ± 63.5	5.10 ± 0.02
NB/NH CaTC	-1.33 ± 0.03	0.06 ± 0.01	625.4 ± 44.7	1.37 ± 0.01
B/300 Ti	-1.39 ± 0.03	0.36 ± 0.03	78.4 ± 0.7	8.29 ± 0.03
B/300 NaTC	-1.40 ± 0.03	0.38 ± 0.23	197.0 ± 100.6	8.79 ± 0.03
B/300 CaTC	-1.36 ± 0.02	0.43 ± 0.04	86.5 ± 9.6	9.93 ± 0.01

date, the presented work was the only such study of titanate coatings being used to modify the corrosion rate of Mg-based materials.

SEM micrographs of the Ti coated (NB/NH Ti and B/300 Ti) and native Mg discs (Fig. 1), demonstrated clear evidence of the magnetron sputtering methodology providing good step coverage, as detailed by Swann [10]. The Ti coating structure appeared to be columnar for all the NB/NH samples, as confirmed *via* XRD (Fig. 6), which is in good agreement with previous work [15], with a preferential orientation in the (002) plane (Ti PDF 00–044–1294) characteristic of such coatings. However, the B/300 samples, exhibited a more equiaxed structure akin to bulk materials [15]. This was due to the increased energy of deposited Ti species by the combination of higher bias and temperature. The presence of the Mg peaks in the sample types tested was due to the X-ray penetration depth being greater than the thicknesses of the produced coatings [34].

There was good agreement between the characterisation techniques used to quantify the Ti coatings deposited on the Mg substrate, however, due to the shallow penetration depth of Raman and XPS, only the top passivated surface layer

(caused by atmospheric exposure) was detected. Raman analysis (Fig. 7) demonstrated clear anatase and rutile modes for both the NB/NH and B/300 Ti samples (similar to bands exhibited in studies by Exarhos [35], Ocana et al. [36], and Hsu et al. [37]), with the NB/NH sample exhibiting a preferred anatase structure, whilst the B/300 Ti had equal anatase and rutile phases. This was expected since the atomic energy provided during the ion-bombardment process was higher in the B/300 sample due to the -100 V bias and 300 °C substrate heating, allowing atomic reordering to occur into the higher energy rutile phase; similar to the findings presented by Simionescu et al. [38]. These peaks were generated from Ti—O bonds, either through vibration, stretching or bending, and can be seen clearly in the XPS spectra presented (Fig. 5). The Ti found within the titania layer, which is due to the passivation of the Ti coating with air, is present in all of the possible valence states: Ti^{4+}, Ti^{3+}, Ti^{2+}, and Ti, however, preferential formation of the Ti^{4+} valence state, akin to TiO_2 (Anatase/Rutile) was noted. The Ti^{3+} valence state was statistically more likely, compared to the Ti^{2+} state due to thermodynamic favourability, as outlined by Hanawa et al. [39].
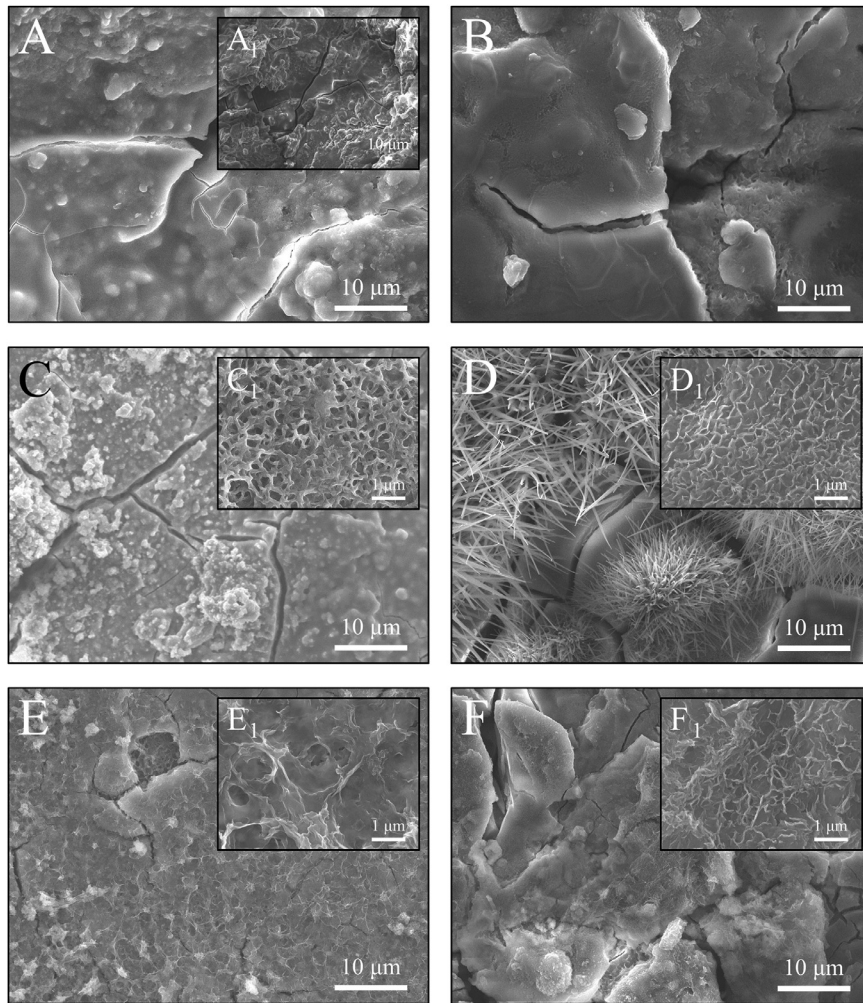
Fig. 9. SEM micrographs of electrochemically degraded samples in DMEM. A) NB/NH Ti with insert $A_1 = Mg$; B) B/300 Ti; C) NB/NH NaTC; D) B/300 NaTC; E) NB/NH CaTC and F) B/300 CaTC. Micrographs A_1, C_1, D_1, E_1 and F_1 are all higher resolution areas of interest, particularly noting regions akin to nanoporous titanate structures.

4.1.2. Sodium titanate conversion

SEM imaging of NB/NH and B/300 NaTC samples (Figs. 1C and 2C) revealed the characteristic nano-porous structure of sodium titanate expected from the chemical treatment used [40]. Successful conversion of the Ti sputtered surface to sodium titanate was supported by EDX (Table 3) and XPS analysis (Fig. 5 and Table 5), both confirming the presence of Na—O. XPS analysis also showed a change in the quantity of deconvoluted Ti 2p doublet peaks, with four doublets of each oxidation state reduced to one doublet of Ti(IV) at 458.5 eV (2p 3/2), characteristic of the TiO_6 octahedral structure of sodium titanate [20]. In addition, Raman spectra (Fig. 7) of both NaTC samples exhibited bands expected of sodium titanate, as detailed by Viana et al. [41] and Zhang et al. [42], further supporting successful conversion. SEM cross-sections (Figs. 1 and 2) detailed two distinct layers in the coating: Ti coating and the sodium titanate structure. The increase in the total thickness of the coating suggests that the titanate structure grows from the Ti base, while the Ti coating reduces in thickness, providing material for titanate growth (Fig. 10). This suggested that the thickness

of the titanate layer was not limited by Ti thickness (> $0.5 \mu m$), and thus the thickness of the sputtered Ti coating could be reduced further and still produce the same thickness of titanate structures. This would not only reduce the coating time, improving efficiency, as well as reducing the residual stress of the coating, which is partially dependant on thickness [43]. The disadvantage of residual Ti in the coating is the possibility of long term complications of Ti metal breakdown [44] as well as galvanic corrosion occurring between Mg and Ti metals [45]. Fig. 10 demonstrated the change in coating thickness upon titanate conversion. Optimisation of the coating would involve the reduction of x_2 to zero, while maximising y_1 thickness *via* minimisation of x_1.

The presence of Ca in XPS and EDX elemental analyses (Table 3), detected in NaTC samples, was suggested to be due to Ca contamination of the NaOH used for hydrothermal conversion; this has been observed in sodium titanate synthesis [46]. Ca^{2+} bonds preferentially, due to increased electrostatic attraction, over Na^+ within the titanate structure, inhibiting the apatite forming ability as a result of the reduced release
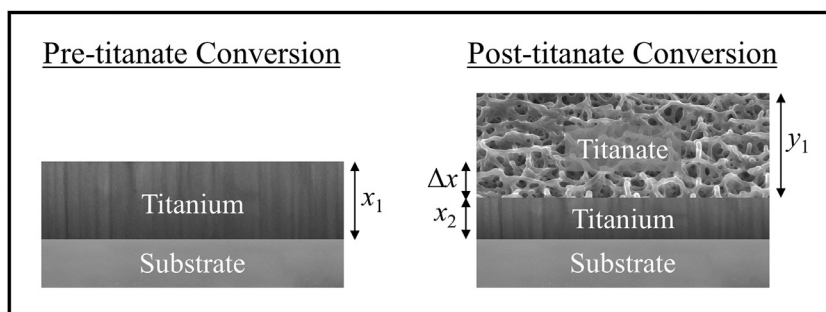
Fig. 10. Schematic of the effect on coating thickness due to titanate conversion of the original titanium coating. x_1 is the original titanium coating thickness, x_2 is the post-titanate converted titanium thickness, Δx is the reduction in Ti thickness or penetration of the titanate layer, x_2 is the new Ti thickness, with y_1 being the thickness of the produced titanate layer.

of Na^+ [46]. Despite this, the confirmation of a sodium titanate layer highlights a novel method for coating Mg substrates with an osteoconductive bioactive surface. A proposed hypothesis from the authors, described the potential for magnesium titanate to form, due to the localised contact between the Ti and Mg surfaces in the presence of an alkaline aqueous environment: if Mg^{2+} ions were present in solution they would exchange with Na^+ ions in the forming titanate due to preferential bonding of multivalent ions [47]. This however was not observed, and suggested that the Mg substrate was passivated with an oxide/hydroxide layer in the presence of the high molarity NaOH (pH > 12), similar to the findings of Lips et al. [48], and Ismail et al. [49].

4.1.3. Calcium titanate ion-exchange

EDX (Table 1) elemental compositions between NaTC and CaTC and XPS elemental analysis (Table 5 and Fig. 5) exemplifies the replacement of Na^+ content for Ca^{2+} for the CaTC samples, indicating successful conversion of sodium titante to calcium titante. XPS further supported this (Table 5 and Fig. 5) due to the loss of the Na 1s peak, the emergence of a clear Ca doublet, as well as a distinct alteration in the realtive peak intensities of the O 1s deconvolutions due to a change in bonding from Ti—O—Na to Ti—O—Ca [50]. The SEM surface images (Fig. 1) possess the same nanoporous morphology as sodium titanate, whilst Raman analysis (Fig. 7) demonstrated the same bands as the NaTC samples, indicative of the isomorphic ionic conversion from sodium to calcium titanate [51,52].

The CaTC samples also exhibited precipitation on their surfaces (Figs. 1E, 2E, and 3), identified as being rich in Ca and O via EDX mapping (supplementary Fig. S1) and XPS analysis (peak position 346.8 eV, from Yaseen et al. [53]), suggesting $Ca(OH)_2$ precipitation due to $Ca(OH)_2$ solution's low solubility [53,54]. This could potentially be resolved through further wash steps within the methodology, however this may cause unnecessary aqueous exposure of the Mg substrate. $CaCl_2$ has previously been used in calcium titanate synthesis [55], however this was deliberately avoided as the presence of Cl^- ions in solution accelerates Mg degradation [56]. $Ca(OH)_2$ has been used in dentistry to promote hard tissue growth in teeth from dissolution of Ca^{2+} and an-

timicrobial activity by increasing local pH [57]. Hence, the presence of this salt could be advantageous in the correct application [44,55,58].

4.2. Electrochemical degradation and delamination analysis

From the preliminary electrochemical degradation data presented, the NB/NH CaTC sample outperformed all other sample types tested. There was a marked increase of 0.16 V compared to the uncoated Mg sample, and an increase of 0.15 V on the Ti coated sample alone. It was hypothesised that the inclusion of calcium within the titanate structure may have a beneficial effect on the corrosion resistance as Ca has been shown to be beneficial in Mg alloying or coatings [59,60]. However, in both B/300 and NB/NH samples, this was clearly not the case with the corrosion potential, E_{corr}, demonstrating no significant difference between the NaTC and CaTC samples. However the E_{corr} results showed a clear qualitative trend for the NB/NH samples: Mg > NB/NH Ti > NB/NH NaTC > NB/NH CaTC.

On the NaTC samples (both NB/NH and B/300) there is a clear increase in the formation of calcium, phosphorous and oxygen rich regions, likely from the DMEM solution used. Titanates produced via aqueous chemical treatments, have the ability to facilitate complex ion-exchange reactions due to their ionic structure, which over time, will form apatite both in SBF in vitro and extracellular fluid in vivo. This ability enables titanates to generate bone, enhancing the adhesion between the osseous-environment and the implant. Combining this property with a degradable material such as Mg, can enhance the bonding of the fracture fixation implant, enabling bone healing to occur at the interface of the fracture ends, whilst also facilitating a more controlled degradation of Mg.

As described by Wei et al. [61], nanorods/nanowhiskers/nanoneedles; all names widely used in the literature for similar structures, can form from MgO, $Mg(OH)_2$, in addition to the more complex $Mg_2(OH)_3Cl \cdot 4H_2O$. As noted in the NB/NH NaTC samples, there is clear formation of Mg, Cl, and O rich (Fig. S1) nanoneedles on the sample's surface, potentially composed of $Mg_2(OH)_3Cl \cdot 4H_2O$, although further comprehensive analysis would be needed to confirm this due to the size of the structures present.

EDX mapping (Fig. 4) of all titanate samples revealed cracking and partial delamination of the coatings to varying degrees. Delamination was due to the release of residual stresses within the Ti sputtered coatings upon conversion to titanate and a poor interfacial strength between the coating and the Mg substrate, even with the use of magnetron sputtering, which is known for good film adhesion [62]. Comparison of relative delamination (Table 4) showed a higher degree of delamination present in the B/300 samples, attributed to the higher residual stresses present in those samples due to the B/300 sputtering parameters [15]. The use of a bias voltage and higher temperature in the sputtering procedure results in higher energy bombardment of the surface by Ti ions, increasing local temperature and the compressive stress of the coating upon cooling.

Both XPS (Table 5) and EDX (Table 3) elemental analyses show the presence of Mg post conversion. As XPS is a surface analysis method, Mg content detected is due solely to delamination of the coating exposing the substrate surface. It must be noted however that the Mg content from EDX measurements was still proportional to the degree of delamination, despite the increased penetration depth. The appearance of Mg bands in the Raman spectra for the NB/NH CaTC sample (Fig. 7) suggests significant delamination of the coating, as the Mg bands are not present in the other titanate sample spectra.

Any degree of delamination is unfavourable for a coating intended to reduce the rate of degradation as it not only exposes the substrate, leaving areas as if untreated, but could create crevices where pitting corrosion could occur [63]. Future work should focus on the elimination of such delamination, which could involve many different routes: the addition of an interlayer to mediate the Ti-Mg interface; reduction of coating thickness minimising residual stress in the coatings; or the use of alloys of magnesium to increase the interface strength to the sputtered Ti and/or increase T_m of the substrate to allow heat treatment to relieve the residual stress before chemical treatment, are a few directions this research could take. Despite the degree of delamination, the NB/NH CaTC sample still performed favourably compared to the Mg substrate alone and exhibited minimal delamination.

5. Conclusions

The demanding paradigm of reducing the degradation rate of magnesium to an acceptable standard for orthopaedic applications has long been a significant issue in biomaterials science. This paper demonstrates the first insights into the tailoring of Mg's degradation rate through the successful application of both sodium and calcium-containing titanate structures, of which, has yet to be achieved in the literature.

Formation of nano-porous surface morphologies characteristic of titanate structures were achieved and determined *via* SEM (surface and cross-section) analysis. The thickness of the Ti layer utilised in this study was thinner than in previous studies (*ca.* 500 nm *vs.* 4 μm), and demonstrated titanate structures of similar thicknesses to previous studies (*ca.* 1.5 μm).

This concluded that an equilibrium state has been achieved both through oxygen penetration and Ti depth (> 0.5 μm), to produce similar titanate thicknesses despite different Ti thickness.

Despite the preliminary data demonstrating the NB/NH CaTC sample provides corrosion protection for Mg substrates ($E_{corr} = ca. -1.33$ *vs.* -1.49 V; $i_{corr} = ca.$ 0.06 *vs.* 0.31 mA.cm^{-2}, respectively), further work is necessary to address the issue of coating delamination, which was exhibited in the majority of samples tested, with the best performing sample type (NB/NH CaTC) exhibited the lowest coating delamination. This can be achieved by either enhancing the interfacial strength of the coating with the Mg substrate, or reducing the residual stress of the sputtered coatings.

Declaration of Competing Interest

The authors declare that they have no known competing financial interests or personal relationships that could have appeared to influence the work reported in this paper.

Acknowledgements

Supplementary materials

Supplementary material associated with this article can be found, in the online version, at doi:10.1016/j.jma.2020.07.001.

References

[1] M. Haghshenas, Mechanical characteristics of biodegradable magnesium matrix composites: a review, J. Magnes. Alloy 5 (2) (2017) 189–201.

[2] C. Godavitarne, A. Robertson, J. Peters, B. Rogers, Biodegradable materials, Orthop. Trauma 31 (5) (2017) 316–320.

[3] M.P. Staiger, A.M. Pietak, J. Huadmai, G. Dias, Magnesium and its alloys as orthopedic biomaterials: a review, Biomaterials 27 (9) (2006) 1728–1734.

[4] M. Pogorielov, E. Husak, A. Solodivnik, S. Zhdanov, Magnesium-based biodegradable alloys: degradation, application, and alloying elements, Interv. Med. Appl. Sci. 9 (1) (2017) 27–38.

[5] Y.Q. Chen, S. Zhao, M.Y. Chen, W.T. Zhang, J.L. Mao, Y.C. Zhao, M.F. Maitz, N. Huang, G.J. Wan, Sandwiched polydopamine (PDA) layer for titanium dioxide (TiO2) coating on magnesium to enhance corrosion protection, Corros. Sci. 96 (2015) 67–73.

[6] A.J. Parsons, R.M. Felfel, M.D. Wadge, D.M. Grant, Improved phosphate-based glass fibre performance achieved through acid etch/polydopamine treatment. Special Issue: Phosphate Glasses and General Glass Science, Int. J. Appl. Glass Sci. 11 (1) (2020) 35–45.

[7] Y. Song, S. Zhang, J. Li, C. Zhao, X. Zhang, Electrodeposition of Ca–P coatings on biodegradable Mg alloy: *in vitro* biomineralization behavior, Acta Biomater. 6 (5) (2010) 1736–1742.

[8] J. Li, Y. Song, S. Zhang, C. Zhao, F. Zhang, X. Zhang, L. Cao, Q. Fan, T. Tang, *In vitro* responses of human bone marrow stromal cells to a fluoridated hydroxyapatite coated biodegradable Mg–Zn alloy, Biomaterials 31 (22) (2010) 5782–5788.

[9] L. Xu, A. Yamamoto, Characteristics and cytocompatibility of biodegradable polymer film on magnesium by spin coating, Colloids Surf. B Biointerfaces 93 (2012) 67–74.

[10] S. Swann, Magnetron sputtering, Phys. Technol. 19 (2) (1988) 67.

[11] P.J. Kelly, R.D. Arnell, Magnetron sputtering: a review of recent developments and applications, Vacuum 56 (3) (2000) 159–172.

[12] S.C. Coe, M.D. Wadge, R.M. Felfel, I. Ahmed, G.S. Walker, C.A. Scotchford, D.M. Grant, Production of high silicon-doped hydroxyapatite thin film coatings via magnetron sputtering: deposition, characterisation, and in vitro biocompatibility, Coatings 10 (2) (2020) 190.

[13] U. Helmersson, M. Lattemann, J. Bohlmark, A.P. Ehiasarian, J.T. Gudmundsson, Ionized physical vapor deposition (IPVD): a review of technology and applications, Thin Solid Films 513 (1–2) (2006) 1–24.

[14] M.A. Surmeneva, T.M. Mukhametkaliyev, H. Khakbaz, R.A. Surmenev, M.B. Kannan, Ultrathin film coating of hydroxyapatite (HA) on a magnesium–calcium alloy using RF magnetron sputtering for bioimplant applications, Mater. Lett. 152 (2015) 280–282.

[15] M.D. Wadge, B. Turgut, J.W. Murray, B.W. Stuart, R.M. Felfel, I. Ahmed, D.M. Grant, Developing highly nanoporous titanate structures via wet chemical conversion of DC magnetron sputtered titanium thin films, J. Colloid Interface Sci. 566 (2020) 271–283.

[16] T. Kokubo, S. Yamaguchi, Bioactive titanate layers formed on titanium and its alloys by simple chemical and heat treatments, Open Biomed. Eng. J. 9 (1) (2015) 29–41.

[17] T. Kokubo, S. Yamaguchi, Novel bioactive materials developed by simulated body fluid evaluation: surface-modified Ti metal and its alloys, Acta Biomater. 44 (2016) 16–30.

[18] D.K. Pattanayak, S. Yamaguchi, T. Matsushita, T. Kokubo, Effect of heat treatments on apatite-forming ability of NaOH- and HCl-treated titanium metal, J. Mater. Sci. Mater. Med. 22 (2) (2011) 273–278.

[19] T. Kokubo, D.K. Pattanayak, S. Yamaguchi, H. Takadama, T. Matsushita, T. Kawai, M. Takemoto, S. Fujibayashi, T. Nakamura, Positively charged bioactive Ti metal prepared by simple chemical and heat treatments, J R Soc. Interface 7 Suppl. 5 (Suppl 5) (2010) S503–S513.

[20] M.D. Wadge, B.W. Stuart, K.G. Thomas, D.M. Grant, Generation and characterisation of gallium titanate surfaces through hydrothermal ion-exchange processes, Mater. Des. 155 (2018) 264–277.

[21] S. Yamaguchi, S. Nath, Y. Sugawara, K. Divakarla, T. Das, J. Manos, W. Chrzanowski, T. Matsushita, T. Kokubo, Two-in-one biointerfaces—antimicrobial and bioactive nanoporous gallium titanate layers for titanium implants, Nanomaterials 7 (8) (2017) 229.

[22] D. Seifzadeh, H.K. Mohsenabadi, Z. Rajabalizadeh, Electroless Ni–P plating on magnesium alloy by innovative, simple and non-toxic oxalate pretreatment and its corrosion protection, RSC Adv. 6 (99) (2016) 97241–97252.

[23] M. Curioni, The behaviour of magnesium during free corrosion and potentiodynamic polarization investigated by real-time hydrogen measurement and optical imaging, Electrochim. Acta 120 (2014) 284–292.

[24] E.J. Catanzaro, T.J. Murphy, E.L. Garner, W.R. Shields, Absolute isotopic abundance ratios and atomic weight of magnesium, J. Res. Nat. Bureau Standards. Section A, Phys. Chem. 70 (6) (1966) 453.

[25] J. Degner, F. Singer, L. Cordero, A.R. Boccaccini, S. Virtanen, Electrochemical investigations of magnesium in DMEM with biodegradable polycaprolactone coating as corrosion barrier, Appl. Surf. Sci. 282 (2013) 264–270.

[26] R.Z. Xu, X.B. Yang, P.H. Li, K.W. Suen, S. Wu, P.K. Chu, Eelectrochemical properties and corrosion resistance of carbon-ion-implanted magnesium, Corros. Sci. 82 (2014) 173–179.

[27] S.N. Dezfuli, Z.G. Huan, J.M.C. Mol, M.A. Leeflang, J. Chang, J. Zhou, Influence of HEPES buffer on the local pH and formation of surface layer during *in vitro* degradation tests of magnesium in DMEM, Prog. Nat. Sci.-Mater. Int. 24 (5) (2014) 531–538.

[28] V. Wagener, S. Virtanen, Protective layer formation on magnesium in cell culture medium, Mater. Sci. Eng. C Mater. Biol. Appl. 63 (2016) 341–351.

[29] X. Gu, Y. Zheng, S. Zhong, T. Xi, J. Wang, W. Wang, Corrosion of, and cellular responses to Mg–Zn–Ca bulk metallic glasses, Biomaterials 31 (6) (2010) 1093–1103.

[30] Y.Y. Yang, C. Michalczyk, F. Singer, S. Virtanen, A.R. Boccaccini, *In vitro* study of polycaprolactone/bioactive glass composite coatings on corrosion and bioactivity of pure Mg, Appl. Surf. Sci. 355 (2015) 832–841.

[31] M.B. Kannan, H. Khakbaz, A. Yamamoto, Understanding the influence of HEPES buffer concentration on the biodegradation of pure magnesium: an electrochemical study, Mater. Chem. Phys. 197 (2017) 47–56.

[32] V. Wagener, S. Virtanen, Influence of electrolyte composition (simulated body fluid *vs.* Dulbecco's Modified Eagle's medium), temperature, and solution flow on the biocorrosion behavior of commercially pure Mg, Corrosion 73 (12) (2017) 1413–1422.

[33] M.K. Arumugam, M.A. Hussein, A.Y. Adesina, N. Al-Aqeeli, In vitro corrosion and bioactivity performance of surface-treated Ti-20Nb-13Zr alloys for orthopedic applications, Coatings 9 (5) (2019).

[34] M. Heshmati, D. Seifzadeh, P. Shoghi, M. Gholizadeh-Gheshlaghi, Duplex Ni-Zn-Cu-P/Ni-P electroless coating on magnesium alloy via maleic acid pretreatment, Surf. Coatings Technol. 328 (2017) 20–29.

[35] G.J. Exarhos, High temperature Raman studies of phase transitions in thin film dielectrics, MRS Online Proc. Library Arch. (1985) 48.

[36] M. Ocana, J.V. Garcia-Ramos, C.J. Serna, Low-temperature nucleation of rutile observed by raman spectroscopy during crystallization of TiO2, J. Am. Ceramic Soc. 75 (7) (1992) 2010–2012.

[37] L. Hsu, R. Rujkorakarn, J. Sites, C. She, Thermally induced crystallization of amorphous-titania films, J. Appl. Phys. 59 (10) (1986) 3475–3480.

[38] O.G. Simionescu, C. Romanitan, O. Tutunaru, V. Ion, O. Buiu, A. Avram, RF magnetron sputtering deposition of TiO2 thin films in a small continuous oxygen flow rate, Coatings 9 (7) (2019) 442.

[39] T. Hanawa, K. Asami, K. Asaoka, Repassivation of titanium and surface oxide film regenerated in simulated bioliquid, J. Biomed. Mater. Res. 40 (4) (1998) 530–538.

[40] H.-M. Kim, H. Takadama, T. Kokubo, S. Nishiguchi, T. Nakamura, Formation of a bioactive graded surface structure on Ti–15Mo–5Zr–3Al alloy by chemical treatment, Biomaterials 21 (4) (2000) 353–358.

[41] B.C. Viana, O.P. Ferreira, A.G. Souza, A.A. Hidalgo, J. Mendes, O.L. Alves, Alkali metal intercalated titanate nanotubes: a vibrational spectroscopy study, Vib. Spectrosc. 55 (2) (2011) 183–187.

[42] Z. Zhang, J.B. Goodall, S. Brown, L. Karlsson, R.J. Clark, J.L. Hutchison, I. Rehman, J.A. Darr, Continuous hydrothermal synthesis of extensive 2D sodium titanate (Na 2 Ti 3 O 7) nano-sheets, Dalton Trans. 39 (3) (2010) 711–714.

[43] H. Oettel, R. Wiedemann, Residual stresses in PVD hard coatings, Surf. Coat. Tech. 76 (1–3) (1995) 265–273.

[44] T. Kokubo, S. Yamaguchi, Simulated body fluid and the novel bioactive materials derived from it, J. Biomed. Mater. Res. A 107 (5) (2019) 968–977.

[45] A.M. Fekry, R.M. El-Sherif, Electrochemical corrosion behavior of magnesium and titanium alloys in simulated body fluid, Electrochim. Acta 54 (28) (2009) 7280–7285.

[46] T. Kizuki, H. Takadama, T. Matsushita, T. Nakamura, T. Kokubo, Effect of Ca contamination on apatite formation in a Ti metal subjected to NaOH and heat treatments, J. Mater. Sci. Mater. Med. 24 (3) (2013) 635–644.

[47] S. Spriano, S. Yamaguchi, F. Baino, S. Ferraris, A critical review of multifunctional titanium surfaces: new frontiers for improving osseointegration and host response, avoiding bacteria contamination, Acta Biomater. 79 (2018) 1–22.

[48] K. Lips, P. Schmutz, M. Heer, P.J. Uggowitzer, S. Virtanen, Electrochemical corrosion investigation on Mg alloy AZ91: description of critical parameters and their influence on the mechanisms of attack on NRC type alloys, Mater. Corros. 55 (1) (2004) 5–17.

[49] K.M. Ismail, S. Virtanen, Electrochemical behavior of magnesium alloy AZ31 in 0.5M KOH solution, Electrochem. Solid St. 10 (3) (2007) C9–C11.

[50] H. Takadama, H.M. Kim, T. Kokubo, T. Nakamura, An X-ray photoelectron spectroscopy study of the process of apatite formation on bioactive titanium metal, J. Biomed. Mater. Res. 55 (2) (2001) 185–193.

[51] S. Yamaguchi, T. Kizuki, H. Takadama, T. Matsushita, T. Nakamura, T. Kokubo, Formation of a bioactive calcium titanate layer on gum metal by chemical treatment, J. Mater. Sci. Mater. Med. 23 (4) (2012) 873–883.

[52] T. Kizuki, T. Matsushita, T. Kokubo, Antibacterial and bioactive calcium titanate layers formed on Ti metal and its alloys, J. Mater. Sci. Mater. Med. 25 (7) (2014) 1737–1746.

[53] S.A. Yaseen, G.A. Yiseen, Z. Li, Elucidation of calcite structure of calcium carbonate formation based on hydrated cement mixed with graphene oxide and reduced graphene oxide, ACS Omega 4 (6) (2019) 10160–10170.

[54] B. Athanassiadis, L.J. Walsh, Aspects of solvent chemistry for calcium hydroxide medicaments, Materials (Basel) 10 (10) (2017).

[55] T. Kizuki, H. Takadama, T. Matsushita, T. Nakamura, T. Kokubo, Preparation of bioactive Ti metal surface enriched with calcium ions by chemical treatment, Acta Biomater. 6 (7) (2010) 2836–2842.

[56] M. Esmaily, J.E. Svensson, S. Fajardo, N. Birbilis, G.S. Frankel, S. Virtanen, R. Arrabal, S. Thomas, L.G. Johansson, Fundamentals and advances in magnesium alloy corrosion, Prog. Mater Sci. 89 (2017) 92–193.

[57] J.J. Morrier, G. Benay, C. Hartmann, O. Barsotti, Antimicrobial activity of Ca(OH)2 dental cements: an *in vitro* study, J. Endod. 29 (1) (2003) 51–54.

[58] Z. Li, X. Gu, S. Lou, Y. Zheng, The development of binary Mg-Ca alloys for use as biodegradable materials within bone, Biomaterials 29 (10) (2008) 1329–1344.

[59] R. Harrison, D. Maradze, S. Lyons, Y. Zheng, Y. Liu, Corrosion of magnesium and magnesium–calcium alloy in biologically-simulated environment, Prog. Nat. Sci. 24 (5) (2014) 539–546.

[60] A.B. Khiabani, A. Ghanbari, B. Yarmand, A. Zamanian, M. Mozafari, Improving corrosion behavior and *in vitro* bioactivity of plasma electrolytic oxidized AZ91 magnesium alloy using calcium fluoride containing electrolyte, Mater. Lett. 212 (2018) 98–102.

[61] Q. Wei, C. Lieber, Solution-based synthesis of magnesium oxide nanorods, MRS Online Proc. Library Arch. 581 (1999).

[62] Y.L. Jeyachandran, B. Karunagaran, S.K. Narayandass, D. Mangalaraj, T.E. Jenkins, P.J. Martin, Properties of titanium thin films deposited by dc magnetron sputtering, Mater. Sci. Eng.-Struct. Mater. Prop. Microstruct. Proc. 431 (1–2) (2006) 277–284.

[63] R. Walter, M.B. Kannan, Influence of surface roughness on the corrosion behaviour of magnesium alloy, Mater. Des. 32 (4) (2011) 2350–2354.